

Received May 31, 2019, accepted July 9, 2019, date of publication July 17, 2019, date of current version August 2, 2019.

Digital Object Identifier 10.1109/ACCESS.2019.2929522

Freehand, Agile, and High-Resolution Imaging With Compact mm-Wave Radar

GUILLERMO ÁLVAREZ-NARCIANDI^{ID}, MIGUEL LÓPEZ-PORTUGUÉS^{ID},
FERNANDO LAS-HERAS^{ID}, (Senior Member, IEEE), AND JAIME LAVIADA^{ID}

Department of Electrical Engineering, University of Oviedo, 33203 Gijón, Spain

Corresponding author: Guillermo Álvarez-Narciandi (alvareznguillermo@uniovi.es)

This work was supported in part by the Ministerio de Educación y Formación Profesional of Spain under the FPU Grant FPU15/06431, in part by the Ministerio de Ciencia, Innovación y Universidades under Project RTI2018-095825-B-I00, and in part by the Principado de Asturias/FEDER under Project IDI/2018/000191.

ABSTRACT The aim of this paper is to present a freehand scanning system with a compact mm-wave radar. In order to achieve high-resolution images, the system exploits the free movements of the radar to create a synthetic aperture. However, in contrast to conventional synthetic aperture radar (SAR), in which canonical acquisition surfaces (e.g., planes or cylinders) are used, the system allows for a given tolerance compatible with real hand-made trajectories. Moreover, different techniques are studied to compensate for the impact of irregular sampling to reduce the artifacts in the image. As a result, real-time scanning can be readily performed even by inexperienced users. The scanning system, comprising a commercial motion capture system and an mm-wave module, can be easily deployed and calibrated. Several results involving different objects are shown to illustrate the performance of the system.

INDEX TERMS SAR imaging, mm-wave imaging, FMCW radar, real-time imaging, freehand scanner.

I. INTRODUCTION

Electromagnetic imaging [1] enables to inspect the inner composition of different objects or beings. This technology can be employed, under different implementations, for nondestructive evaluation of materials [2], [3], medicine [4], defense and security [5]–[7], food inspection [8], [9], obstacle detection [10], among other applications.

A very desirable feature for any of the previous system is compactness. This feature is obviously linked to the working frequency and, therefore, it is hard to achieve in microwave systems. However, *mm-wave* systems can be very compact enabling on-chip systems [11], [12] at the expense of some penetration capabilities. Moreover, the quick development of this technology in the last years has enabled a wide variety of robust and affordable devices.

Although the range resolution depends on the bandwidth, which does not impose a specific size limitation, the lateral resolution of a mm-wave imaging system is proportional to the size of the aperture of the system. Consequently, although a single transmitter and receiver system can be relatively small, high resolution imaging requires of relatively bulky

structures formed by large antennas based on reflectors or lenses [13], raster scanning along well-known paths [5] or large arrays [14].

A balance between system size and resolution has been recently presented in [15] implementing a portable microwave camera operating from 20 to 30 GHz. Furthermore, this kind of system can take advantage of multi-view approaches to increase the imaged area and the image quality [16]–[19].

In this paper, compactness is moved a step forward by performing high-resolution imaging with a single *radar-on-chip*. For this purpose, the radar is moved over the volume to be imaged to build a synthetic aperture.

In order to apply the imaging algorithm in real-time, the position of the radar is tracked by means of a motion capture system. It is interesting to observe that this kind of tracking was already successfully employed to directly map electromagnetic sources for electromagnetic compatibility purposes using a 3D manual scanning [20]. In a similar fashion, the tracking system was also used to indirectly map sources by means of backpropagation using a manual scanning system constrained to two dimensions [21]. A study of the feasibility of using inertial navigation systems for imaging applications has been presented in [22].

The associate editor coordinating the review of this manuscript and approving it for publication was Laxmisha Rai.

In the context of electromagnetic imaging, freehand scanning constrained to two dimensions has also been demonstrated in [23] by implementing a system in the X-band and using a railway system to track the position. However, to the best authors' knowledge, it is the first time that a completely 3D freehand scanning with such a compact device is presented.

This paper is organized as follows. First, the structure of the scanner and its workflow is presented. Second, the radar processing implemented in the demonstrator is explained. Next, the results of several simulations performed to assess the impact of positioning errors and nonuniform sampling in the scanner results are summarized. After that, the calibration procedure for the radar system is introduced and the obtained measurement results are presented. Finally, the conclusions are drawn.

II. FREEHAND MM-WAVE IMAGING

A. SYSTEM ARCHITECTURE

The scanning system main goals, which imply several challenges in terms of positioning accuracy and data processing algorithms, are the following:

- High resolution images: in order to provide high resolution images with a *compact* system, a radar module in the mm-wave band is chosen. In addition, the measurements are acquired along a *synthetic aperture* and coherently combined to improve the resolution. For this purpose, the position of the radar must be acquired with an accuracy much smaller than the wavelength, i.e., submillimeter position accuracy is required.
- Freehand system: the scanner must build the images while it is freely moved so that the operator can dynamically choose the areas where to spend more time scanning to refine the image. As a consequence, due to the nature of the freehand movement of the scanner, the measurements of the radar are not expected to be uniformly spaced.
- Real-time operation: the measurements must be processed on-the-fly and the image must be updated as more data is acquired by the scanner.

In order to provide the previous functionalities, the scanning system, whose scheme is depicted in Fig. 1, was structured in three subsystems:

- Control and processing subsystem: it is in charge of setting up the scanning system, i.e., establishing the communication with the other two subsystems and defining the volume under test, in which the reflectivity will be computed to create the radar images in real-time. In addition, the control subsystem is responsible for querying both the radar frames and the position of the radar, and processing the obtained information, as illustrated in the workflow depicted in Fig. 2. This subsystem is formed by a conventional PC or a laptop, which is interfaced with the radar subsystem with a USB

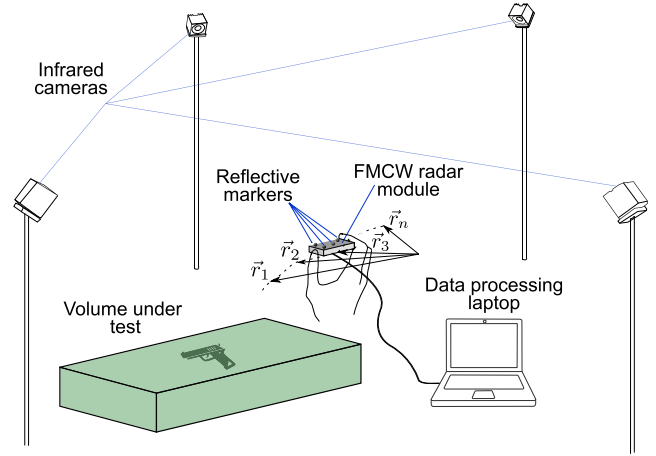


FIGURE 1. Scheme of the proposed scanning system.

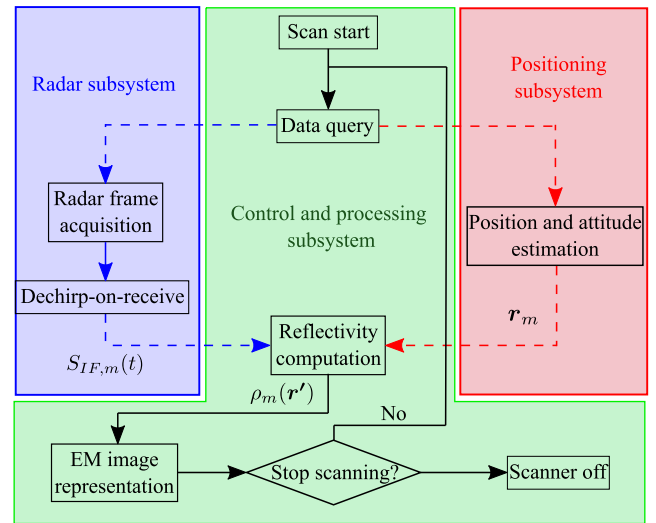


FIGURE 2. Workflow of the scanning system.

cable and with the positioning subsystem by an Ethernet connection.

- Radar subsystem: it comprises a commercial FMCW mm-wave radar module, in this case the radar-on-chip BGT60TR24B by Infineon® [11]. This subsystem transmits and receives the radar signals on demand of the control subsystem enabling the acquisition of the IF signal for further processing. The frequency waveform of the signal transmitted by the radar has an up-chirp saw tooth pattern centered at $f_c = 60$ GHz with a bandwidth of $BW = 6$ GHz and a chirp duration of $T_s = 512 \mu s$. The RF frontend includes 2 transmitting and 4 receiving antennas. However, for this system a *quasimonostatic* configuration, with one transmitting and one receiving antenna, was considered. The radar module was embedded in a 3D-printed enclosure designed ad-hoc for it to ease the manipulation of the radar as well as to help in the placement of the reflective markers of the positioning system (Figs. 3a and 3b).

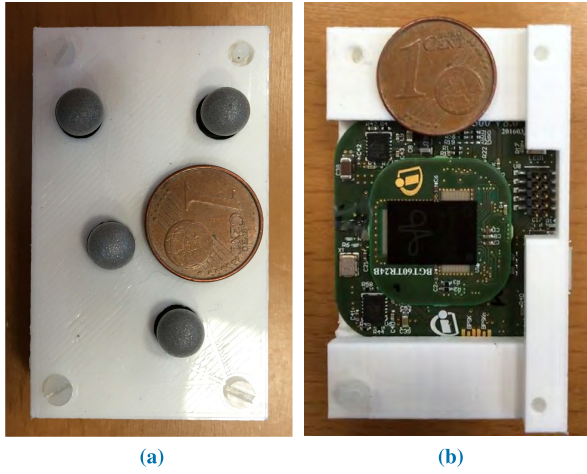


FIGURE 3. Radar module enclosure: (a) top view and reflective markers for the positioning system (b) and bottom view. A one euro-cent coin is included for scale purposes.

- Positioning subsystem: it estimates the position and the attitude of the radar module by means of an optical tracking system. This subsystem is formed by the motion capture system of Optitrack® [24]. The infrared cameras of the system track the reflective markers attached to the radar module (see the scheme of the system in Fig. 1). The position retrieved by the positioning system, which is the centroid of the rigid body defined by the deployed markers, must be corrected to match the position of the radar as the described in Section III-D. This commercial setup, which requires a minimum of four cameras, can be easily deployed and calibrated in a matter of minutes.

B. IMAGING TECHNIQUE

Due to the freehand nature of the proposed imaging system, the acquired data are not expected to be equally spaced along a canonical geometry as it is usually assumed in conventional synthetic aperture radar (SAR) techniques [25]. For this reason, a *delay and sum* algorithm, adapted to the particularities of the FMCW radar signal, is used.

In order to update the image, which shows the reflectivity of the scene, the algorithm requires the current radar position \mathbf{r} and the previous dechirped signal provided by the radar module (see workflow in Fig. 2). Since the signal transmitted by the radar, expressed in complex form, is given by

$$s_{tx}(t) = e^{j2\pi(f_c t + \frac{1}{2}\alpha t^2)}, \quad (1)$$

where $|t| < T_s/2$ and

$$\alpha = \frac{BW}{T_s}, \quad (2)$$

is the slope rate, then if a point target is assumed, the signal received by the radar, without considering amplitude variations, will be given by a delayed version of the transmitted signal

$$s_{rx}(t) = s_{tx}(t - \tau) = e^{j2\pi(f_c(t-\tau) + \frac{1}{2}\alpha(t-\tau)^2)}, \quad (3)$$

where τ is proportional to the distance from the radar position to the point target (R):

$$\tau = \frac{2R}{c}. \quad (4)$$

Thus, the input dechirped signal, obtained by mixing the received and transmitted signals [26], [27] will be given by:

$$s_{IF}(t) = e^{j2\pi(\alpha\tau t + f_c\tau - \frac{1}{2}\alpha\tau^2)}, \quad (5)$$

which has beat frequency $f_b = \tau\alpha$. If the object under test is not a point target but a *distributed target*, then the received signal can be expressed as a superposition of signals given by (3) and so will be the IF signal. In practice, the radar does not return the complex signal in (5) as it lacks of an IQ mixer. However, thanks to the wideband nature of the signal, the analytic signal can be easily retrieved by means of an efficient Hilbert transform [28].

The reflectivity ρ at each point \mathbf{r}' of the grid in which the volume under test is discretized is estimated by coherently summing the contribution of the signal received by the radar at each acquisition position. In order to achieve this coherent combination, the extra phase term, which can be approximated by $f_c\tau - \frac{1}{2}\alpha\tau^2 \approx f_c\tau$ for close targets, is firstly compensated and, after that, a range compression is performed by doing a Fourier transform in the time domain. Thus, the following auxiliary signal is firstly constructed at each radar position for each observation position \mathbf{r}' :

$$s_{c,m}(\mathbf{r}', f) = \mathcal{F} \left\{ s_{IF,m}(t) e^{-j2\pi f_c \tau_m(\mathbf{r}', \mathbf{r}_m)} \right\}, \quad (6)$$

where $\mathcal{F}\{\cdot\}$ denotes the Fourier transform operator and $s_{IF,m}(t)$ is the IF signal acquired at the m -th radar position denoted by \mathbf{r}_m and $\tau_m(\mathbf{r}', \mathbf{r}_m) = 2 \frac{\|\mathbf{r}' - \mathbf{r}_m\|_2}{c}$, which is the propagation delay between the radar position and the observation point.

This auxiliary signal will peak at the beat frequency, which is expected to be proportional to the distance to the target

$$f_{b,m} = \alpha\tau_m = \frac{2\alpha \|\mathbf{r}' - \mathbf{r}_m\|_2}{c}, \quad (7)$$

and, therefore, standard time-domain techniques, similar to the ones used in UWB imaging (e.g., [29], [30]), can be used. In particular, the following delay and sum algorithm can be formulated with a simple change of variable:

$$\rho_m(\mathbf{r}') = \sum_{i=1}^m s_{c,i}(\mathbf{r}', \frac{2\alpha \|\mathbf{r}' - \mathbf{r}_i\|_2}{c}), \quad (8)$$

Although this algorithm is not as efficient as other implementations relying on Fast Fourier Transforms (e.g., [31]) but requiring equally spaced data, it is still able to provide real-time reflectivity estimations for areas of several squared centimeters as it will be illustrated later.

III. PRACTICAL CONSIDERATIONS

Conventional imaging algorithms are applied to data acquired at equally-spaced positions over canonical geometries (e.g., [5], [25]). Although the scanning system can take samples at very regular intervals, due to the lack of a perfectly steady hand, the samples will not be equally spaced. Moreover, the relatively arbitrary trajectories do not guarantee to cover a given surface with a single pass. This results in a number of issues to be solved or mitigated.

A. SAMPLES DISTRIBUTION

The acquired samples will not be equally spaced along a canonical surface. In this paper, the ideal target surface is a *plane*. Depending on the movement speed, more or less samples will lay on some specific areas. This could result in areas of the image with reflectivity levels higher than other areas because of this imbalance in the sample density.

In order to mitigate this issue, the flat surface is split into squared *macrocells* and only a pre-established number of samples are used by the imaging algorithm in each macrocell. This situation is shown in Fig. 4, in which only two samples per macrocell are used by the imaging algorithm independently on the number of samples acquired inside the macrocell.

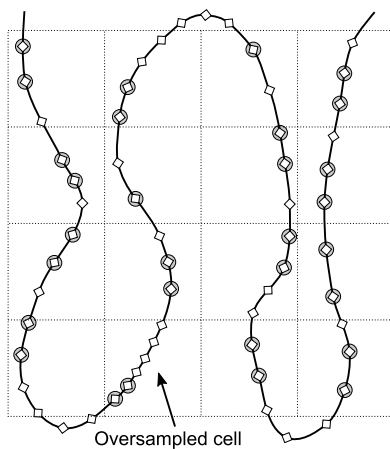


FIGURE 4. Distribution of the acquisition points for the imaging algorithm: Diamonds denote acquisition points and gray circles denote points used by the imaging algorithm.

As a complement to assist during the scanning, the amount of samples per macrocell is shown in a 2D image similar to a *heat map* so the operator can easily check the amount of available data along the scanning surface.

In the presented implementation, the size of the macrocells is chosen as $1 \times 1 \text{ mm}^2$ and the number of samples per cell is set to 3. During the data acquisition, it is not possible to foresee if the scanner will move back to a cell, providing the opportunity to acquire samples well-spaced in the cells. For this reason, a simple algorithm based on retaining the first samples is used.

B. ACQUISITION ALONG A NON-FLAT SURFACE

Despite the previous strategy, the samples will not be perfectly distributed and, therefore, some impact is expected in

the image. Moreover, although scanning along a flat surface is targeted, some flexibility must be granted to the operator, who cannot describe perfectly bidimensional trajectories.

In order to assess the effect of these issues, several systematic simulations were conducted using the IF signal model given by (5). For this purpose, an ideal target with the shape of the letter “T” was defined and several simulations were performed randomizing the horizontal positions and height where the samples were taken. First, a 2D regular grid of sampling locations was defined in order to obtain a reference reflectivity image (Fig. 5a). Then, 3D random variations to the regular sampling positions were generated using a normal distribution for several variance values. The obtained results keeping the horizontal distribution of the regular grid points but adding height variations according to a normal distribution of $\sigma = 1 \text{ cm}$, $\sigma = 1.5 \text{ cm}$ and $\sigma = 2 \text{ cm}$ are depicted in Figs. 5b, 5c and 5d, respectively. As can be observed, after adding height variations to the sampling points originally distributed in a regular grid contained in a flat surface, the image is noisier and some artifacts appear the more nonuniformity is introduced in the sampling positions. However, the quality of the retrieved reflectivity image, though degraded, still enables to clearly recognize the test object.

An analogous analysis was performed modifying both height and horizontal position. As can be seen in Fig. 5e, retrieved with the sampling positions depicted in the *heat map* of Fig. 5g, which were obtained modifying the original sampling grid with a normal distribution of $\sigma = 1 \text{ cm}$ in each horizontal direction, and in Fig. 5f, in which the height of the sampling positions depicted in Fig. 5g was also modified using a normal distribution of $\sigma = 1 \text{ cm}$, the results are similar to those previously presented in this section. Hence, it is possible to conclude that, although due to the nonuniform sampling the resulting reflectivity images are noisier and some artifacts appear, the retrieved image is still accurate.

In order to allow for height variations in a certain tolerance range, the macrocells are extended from 2D rectangles to cuboids. According to the previous study, a small height tolerance would result in better quality images but many samples would be discarded due to the small size and, therefore, the overall scanning time would be increased as many areas should be resampled. Moreover, as it will be analyzed next, other factors such as the positioning error have also an impact, which can be a more limiting factor. In this work, squared macrocells of 1 mm of side and a height tolerance of $\pm 1 \text{ cm}$ were considered.

C. IMPACT OF POSITIONING ERROR

Positioning errors arise from two reasons (assuming that the errors due to the accuracy of the optical tracking system can be neglected compared to them):

- 1) Calibration error: the optical tracking system provides the position of the centroid of the markers attached to the radar enclosure. As a consequence, there is an offset between the position estimated by the localization system and the radar position, which has to be

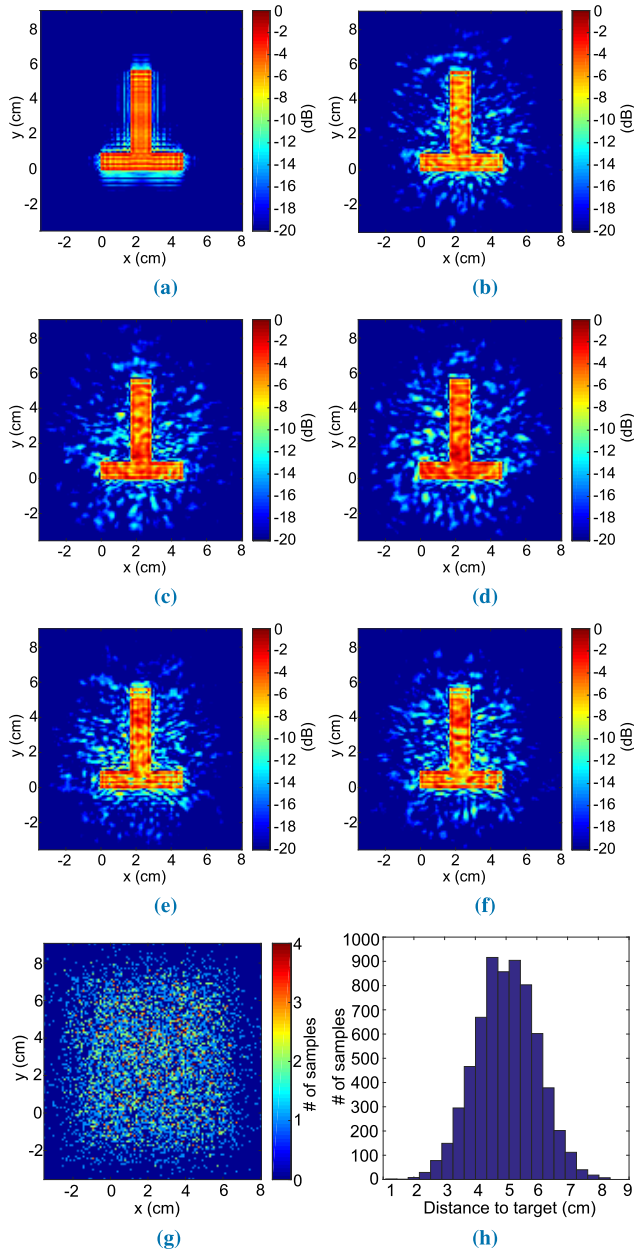


FIGURE 5. Reflectivity image of the simulated target computed with (a) uniform sampling and without positioning errors. Reflectivity image computed modifying the height of the regular positions by adding values obtained using a normal distribution of (b) $\sigma = 1$ cm, (c) $\sigma = 1.5$ cm and (d) $\sigma = 2$ cm. Reflectivity image obtained for (e) nonuniform sampling positions in a 2D plane and also (f) modifying the height of the sampling positions. The heat map of the simulated radar positions used to obtain images (e) and (f) is depicted in (g) and the histogram of the height of the simulated radar positions used to compute (f) is shown in (h).

estimated in a calibration stage. During the scanning process, the position estimated by the optical tracking system has to be corrected taking into account the previously estimated offset and the attitude of the rigid body defined by the reflective markers.

- 2) Delay between the radar acquisition and the position query: during the scanning process, the position of the

radar and the radar data are requested simultaneously. However, since they are independent systems, a perfect synchronization is not guaranteed. Therefore, the position of the radar module when the radar data is acquired can be slightly different to its position when the tracking system was queried.

The impact of the calibration error will be firstly studied by evaluating its effect for the same ideal target shown in Fig. 5a. For this purpose, several simulations for different values of the offset between the radar position and the centroid of the reflective markers, denoted by \mathbf{w} , were performed.

At this point, it is relevant to observe that the attitude of the radar, in terms of yaw, pitch and roll (φ , θ and ψ , respectively), plays a relevant role in this study as the magnitude of the error, in each dimension is given by

$$\epsilon_{cal} = \mathbf{R}(\varphi, \theta, \psi)\mathbf{w}, \quad (9)$$

where $\mathbf{R}(\varphi, \theta, \psi)$ is the rotation matrix computed for the attitude angles of the rigid body defined by the reflective markers provided by the tracking system [32]. If the attitude angles were constant along the scanning, then the *relative* position between the acquired sampling points, even for high errors in the estimation of \mathbf{w} , would be error free. Moreover, it is straightforward to prove that the higher the range of the attitude angles along the scan, the higher the error between real and the estimated radar positions (Fig. 6). For this reason, a threshold for the maximum values of the attitude angles is used in these simulations. This threshold will be the same for all the angles and will be denoted by θ_{max} . This threshold can be easily implemented in measurements by discarding those positions where at least one attitude value is outside the range $\pm\theta_{max}$.

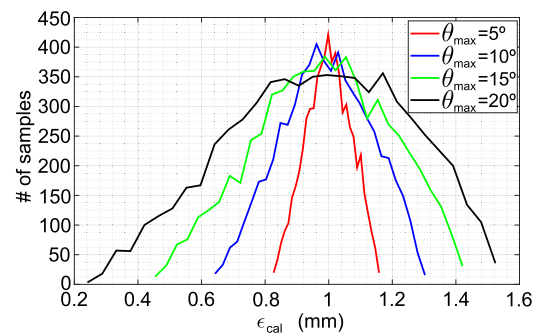


FIGURE 6. Histogram of the error between the real and the estimated radar position in the x-axis for 6536 observations, $\mathbf{w} = (1, 1, 1)$ mm and different values of yaw, pitch and roll generated using a uniform distribution $[-\theta_{max}, \theta_{max}]$.

The obtained results are summarized in Fig. 7, where, as expected, the greater the offset is, the worse is the quality of the reconstructed image. This can be easily checked comparing Figs. 7a and 7c for $\mathbf{w} = (1, 1, 1)$ mm and $\mathbf{w} = (2, 2, 2)$ mm respectively. The same holds for the maximum value of the attitude angles of the scanner, which can be seen comparing Figs. 7c and 7g. Both images were obtained for an offset value of 2 mm in each of the three coordinate axes

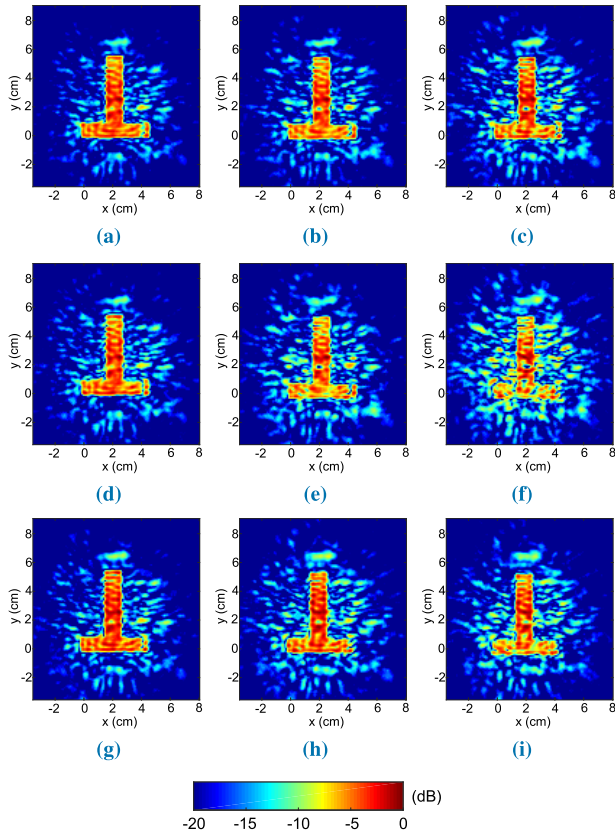


FIGURE 7. Reflectivity image of the simulated target computed for $w = (1, 1, 1)$ mm and $\theta_{max} = 10^\circ$ (a), $w = (1, 2, 1)$ mm and $\theta_{max} = 10^\circ$ (b), $w = (2, 2, 2)$ mm and $\theta_{max} = 10^\circ$ (c), $w = (1, 1, 3)$ mm and $\theta_{max} = 10^\circ$ (d), $w = (1, 3, 1)$ mm and $\theta_{max} = 10^\circ$ (e), $w = (3, 3, 1)$ mm and $\theta_{max} = 10^\circ$ (f), $w = (2, 2, 2)$ mm and $\theta_{max} = 5^\circ$ (g), $w = (3, 3, 3)$ mm and $\theta_{max} = 5^\circ$ (h) and $w = (4, 4, 2)$ mm and $\theta_{max} = 5^\circ$ (i).

but the quality of Fig. 7c, obtained for $\theta_{max} = 10^\circ$ is lower than the quality of Fig. 7g, which was obtained for $\theta_{max} = 5^\circ$. It should be pointed out that, as can be observed comparing Figs. 7d and 7e, an offset in one of the axes parallel to the area under scan has a higher impact on the quality of the obtained images than an offset in the axis in the orthogonal direction.

In conclusion, the maximum value of each attitude angle, which can be controlled by software discarding the measurements taken when the attitude of the scanner is over a given threshold, should be imposed taking into account the maximum accuracy of the offset between the radar position and the centroid of the reflective markers that can be achieved during the calibration procedure. According to our experience, a value of 5° provides a good trade-off between scanning speed and image quality.

The second positioning error, related to the synchronization imperfections, can be mitigated following an approach similar to the ones previously used. Thus, the position can be acquired before polling the radar and after retrieving the radar data. If the distance between the two positions is larger than a given threshold, this data can be discarded. This situation usually happens if the radar module is moved too fast.

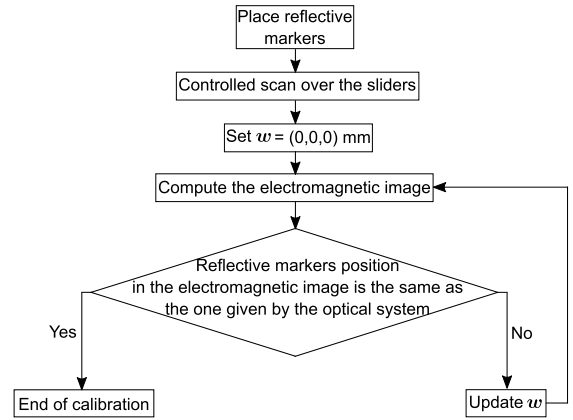


FIGURE 8. Workflow of the calibration procedure.

This analysis will be performed with real data in the Results section.

D. POSITIONING SYSTEM CALIBRATION

As previously stated, the optical tracking system provides the position of the centroid of the reflective markers attached to the radar enclosure. As a consequence, there is an offset between the position provided by localization system and that of the radar. This offset must be estimated in order to correct the position estimations of the tracking system and coherently combine the radar measurements. The calibration procedure, summarized in Fig. 8, consists of the following steps:

- 1) The radar enclosure is mounted onto a support structure, which is adjusted to be moved over a platform with two sliders (Fig. 9a). Thus, the scanner can be moved only over a plane parallel to the area under scan and the attitude angles are fixed.
- 2) Several reflective markers (Fig. 9b) are placed in the area under scan and their positions are measured with the optical tracking system.
- 3) A scan was performed moving the radar along the sliders.
- 4) The offset values for each axis are initially zero and, after that, they are optimized until the position of the reflective markers in the electromagnetic image matches the one given by the optical tracking system and the maximum of the reflectivity is inside the plane which corresponds to the actual vertical coordinate of the markers.

The offset values obtained after the calibration are $w = (-2, -5.4, 12)$ mm. The reflectivity image for the three markers before and after the calibration are depicted in Figs. 9c and 9d respectively. As can be seen, after the calibration, the three areas with high reflectivity, i.e., the markers of the tracking system, were shifted to the location of the markers given by the tracking system. In addition, the amount of noise was reduced, the image was better focused and the shape of the markers is circular, as their actual shape. It should

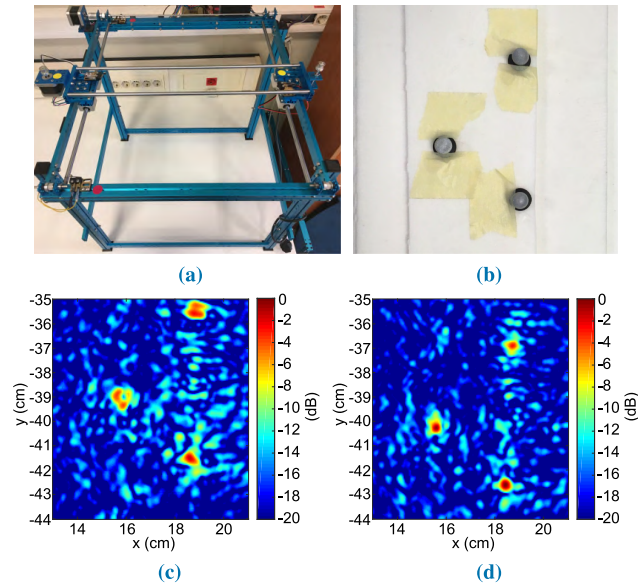


FIGURE 9. Calibration platform with the sliders (a), reflective markers used to calibrate the scanner (b), reflectivity image obtained before the calibration (c) and after the offset w was estimated (d).

be noticed that the calibration must be done only once when the radar is attached to the reflective markers.

IV. RESULTS

Several measurements were conducted to assess the performance of the system. In order to help the system operator during the scanning process, several visual aids were displayed in the interface of the control laptop. In particular, the attitude angles and the height of the scanner provided by the tracking system are depicted along the heat map to control the number of samples acquired over each part of the volume under test.

First, a test with a letter “T” foiled with metal was used as test target in order to compare the measurement results with the numerical results presented in Section III-C. Second, a test with a mannequin and a gun, resembling a security application, was performed. In each case, the volume under test was defined by means of a 3D point grid, which was divided in a set of planes, where the reflectivity was computed. During the scanning process, the electromagnetic image, i.e., the reflectivity computed in one of the planes in which the volume under test was divided, is shown to the operator along the heat map with the sampling information. The operator can interactively change the plane whose reflectivity is being depicted so as to focus the electromagnetic image on the desired target. All the measurements were performed using a laptop for both controlling the scanner and processing the acquired data. This laptop was equipped with a Intel® i7-7700HQ (2.8 GHz), 16 GB of RAM and a NVIDIA® GeForce GTX 1050 graphic card.

A. TEST TARGET

A 3D test target with the shape of the letter “T” (Fig. 10a) was scanned with the radar. The positions at which radar

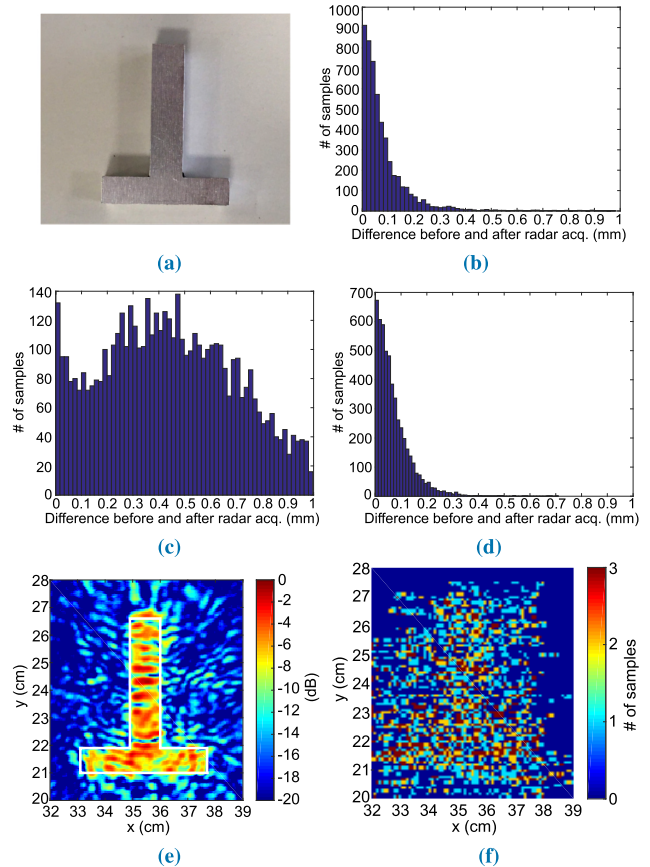


FIGURE 10. Letter used as a test target (a), histogram of the difference between the positions estimated before and after the radar acquisition in the y -axis (b), in the x -axis (c) and in the z -axis (d), reflectivity image obtained after the scan (e) and heat map depicting where the radar data was acquired (f).

acquisitions were performed are depicted in Fig. 10f and the reflectivity image is shown in Fig. 10e, where the contour of the scanned letter is plotted with a white line. The reflectivity was estimated in a set of 8 planes of $22 \times 10 \text{ cm}^2$, the total acquisition time was 297 s and the update frame rate of the image was 25.2 frames per second. The average distance from the radar to the target was 5.27 cm. As can be seen, the test letter is well-reconstructed being the quality of the image comparable to Figs. 7b, 7d and 7h.

In addition, an analysis of the upper bound of the error, due to the delay between the position estimation and the radar acquisition, was performed. In order to do so, the workflow of the scanner was modified to query its position to the tracking system before and after the radar acquisition. Hence, an upper bound of the error can be obtained by computing the difference between the two position estimations (measurements for which the difference between the two position acquisitions was greater than 1 mm were discarded by software). The histograms of the absolute value of the difference between the two position acquisitions are depicted in Figs. 10b and 10c for each of the axes of the plane parallel to the volume under test and in Fig. 10d for

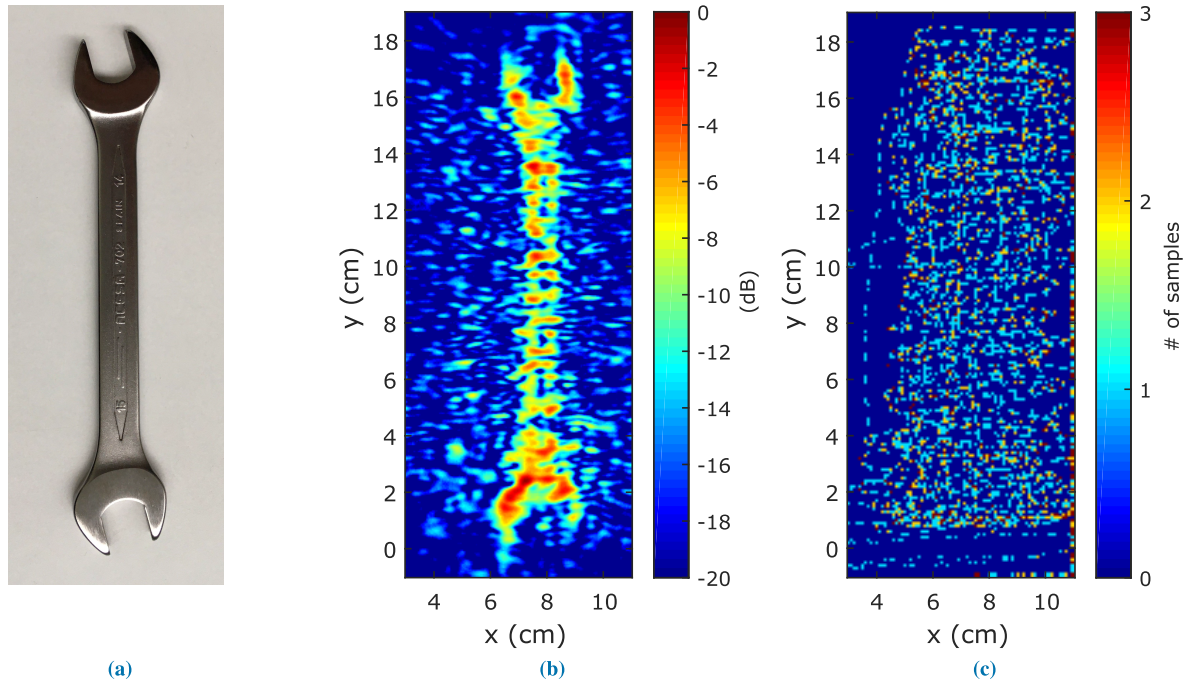


FIGURE 11. Image of the (a) hand wrench used as a target, (b) reflectivity obtained after the scan and (c) heat map depicting where the radar data was acquired.

the orthogonal direction. As can be seen, the displacement upper bound for nearly all the acquisitions is below 0.3 mm in Figs. 10b and 10d. However, as expected, this upper bound is higher in the axis of the main movement direction of the *s-shape* path described with the scanner during the data acquisition (Fig. 10c). In order to limit this upper bound, the speed of the scanning process is limited by software. As previously described, this can be achieved by discarding the radar data when the difference between the two position acquisitions explained before is greater than a given distance. Particularly, this distance was set to 2 mm for the tests presented in this manuscript.

B. TEST WITH A HAND WRENCH

Another example to illustrate the performance of the system was carried out with the hand wrench depicted in Fig. 11a. The positions at which radar acquisitions were performed are depicted in Fig. 11c and the obtained reflectivity image is shown in Fig. 11b.

In this case the reflectivity was computed in a set of 7 planes of $11 \times 22 \text{ cm}^2$ during a total acquisition time of 269 s. The update rate of the reflectivity image was 26.2 frames per second and the average distance from the radar to the target was 7.8 cm. As can be seen, the handle of the wrench and both of its open ends are well-reconstructed. Also, it is worth noting that there is a lower reflectivity value in the central part of the handle, where the thickness of the wrench is lower.

C. TEST WITH A MANNEQUIN

The setup comprising the mannequin and the gun is depicted in Fig. 12a and a zoomed view of the imaged gun is shown

in Fig. 12b. As can be seen, the mannequin is covered by aluminum foil as it provides a fair representation of the human skin at mm-wave frequencies. In addition, it should be pointed out that this is a worse situation than using a more realistic model of the skin since the contrast between the body and the metal of the gun would be higher. The reflectivity was estimated in a set of 11 planes of $18.6 \times 12.7 \text{ cm}$, the total acquisition time was 1162 s and the update frame rate of the image was 15.5 frames per second (it should be noted that the lower update rate is due to the increase of the reconstruction volume). The average distance from the radar to the target was 5.8 cm. It should be pointed out that the proposed system was implemented in MatLab[®] and could be further optimized to increase the framerate (which would also speed up the samples acquisition). Furthermore, the acquisition time could be drastically reduced using more than one receiving antenna, i.e., by taking samples at more than one location for each position of the scanner. To give an idea of the increasing number of receivers that manufacturers are integrating in a single chip, Vayyar has recently announced a chip with 72 transmitters and 72 receivers [33]. The results are plotted in Fig. 12c, where the color of each pixel of the 2D image is proportional to the depth of the point with highest reflectivity within all the planes in which the volume under test was divided. Moreover, the brightness of each pixel was weighted by the reflectivity magnitude corresponding to it [18]. The heat map depicting the horizontal positions where the radar acquisitions were performed is shown in Fig. 12d. Although the trigger is not detected (it is closer to the mannequin than the rest of the gun, i.e., the height difference between the background and the trigger is smaller, and its size is smaller), the shape of the pistol is well-reconstructed.

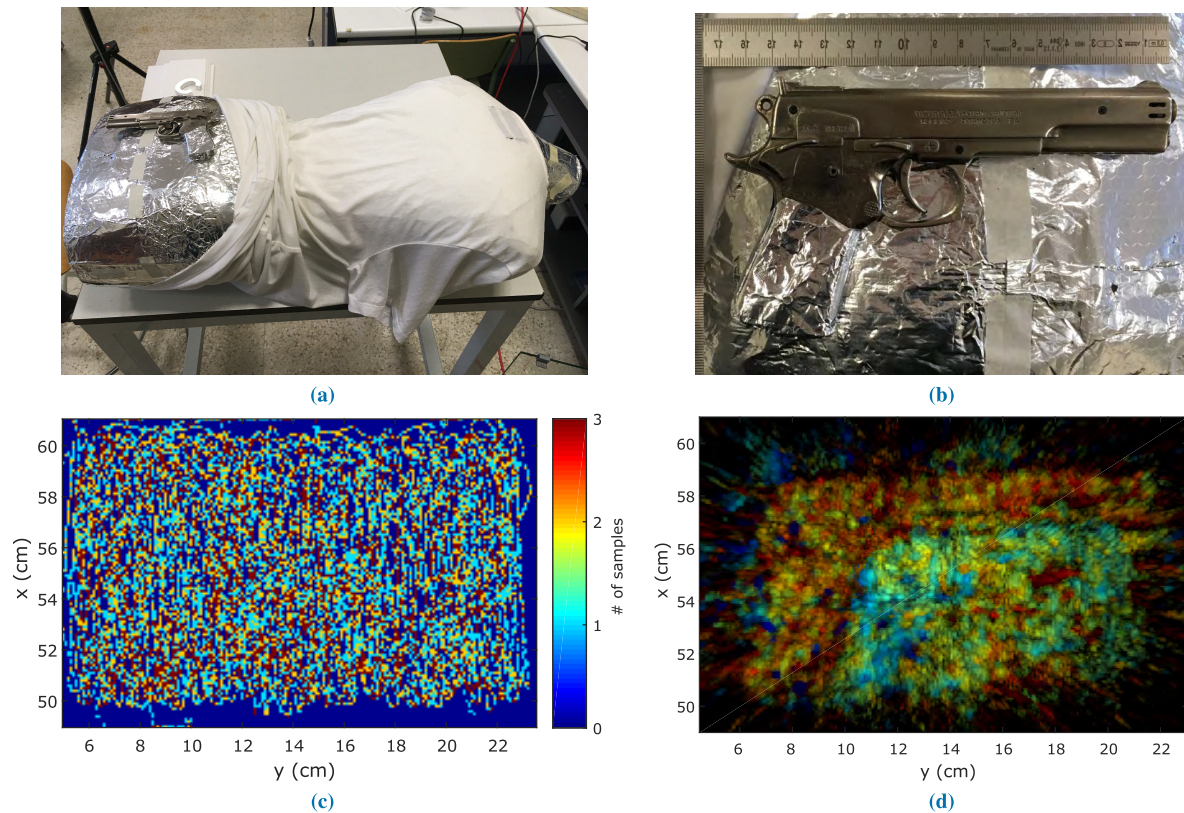


FIGURE 12. Image of the (a) mannequin with an attached gun, (b) the imaged gun zoomed, (c) heat map depicting where the radar data was acquired, and (d) reflectivity image obtained after the scan.

V. CONCLUSION

In this manuscript a mm-wave freehand scanner based on a FMCW radar was presented. The proposed system also comprises an optical tracking system to estimate the position of the radar and a conventional laptop to process the measurements using a delay and sum algorithm to obtain high-resolution real-time reflectivity images.

The main focus of the manuscript was devoted to present the architecture of the system, to assess the problems that arise due to the real-time operation and freehanded movement of the scanner and how to overcome and mitigate them and to evaluate the performance of the system with several test targets. In particular, the effect of nonuniform sampling and positioning errors was addressed by means of simulations. Results show that nonuniform sampling and positioning errors cause an increase of noise in the reflectivity image and the appearance of some artifacts and, hence, some strategies to mitigate these effects were developed (restricting the maximum value of the attitude of the radar, dividing the volume under test in 3D macrocells and controlling the synchronization of the tracking system and the radar). However, the main source of error are positioning errors which, in the presented prototype, are mainly due to calibration errors. At this point, it should be remarked that this problem could be drastically reduced with an industrial fabrication of the scanning system (comprising the radar and the markers).

Regarding the real-time performance of the system, several radar acquisitions are buffered prior to the reflectivity update to speed up the system and results show that high update rates for the reflectivity image can be achieved. In spite of that, higher volumes under test slow down the update rate of the scanner and the required time to scan middle size areas (hundreds of seconds) limits the direct usage of the presented prototype for some of its potential applications. However, the presented prototype paves the way for ultrafast scans as the processing algorithm can be optimized and the number of transmitters and receivers in the radar chip can be increased to speed up the data acquisition. Finally, the laboratory tests show that both simple and complex targets can be imaged and high-resolution reflectivity estimations can be obtained.

REFERENCES

- [1] M. Pastorino, *Microwave Imaging*. Hoboken, NJ, USA: Wiley, 2010.
- [2] S. Kharkovsky, J. T. Case, M. A. Abou-Khousa, R. Zoughi, and F. L. Hepburn, "Millimeter-wave detection of localized anomalies in the space shuttle external fuel tank insulating foam," *IEEE Trans. Instrum. Meas.*, vol. 55, no. 4, pp. 1250–1257, Aug. 2006.
- [3] F. Boero, A. Fedeli, M. Lanini, M. Maffongelli, R. Monleone, M. Pastorino, A. Randazzo, A. Salvadè, and A. Sansalone, "Microwave tomography for the inspection of wood materials: Imaging system and experimental results," *IEEE Trans. Microw. Theory Techn.*, vol. 66, no. 7, pp. 3497–3510, Jul. 2018.
- [4] N. K. Nikolova, "Microwave imaging for breast cancer," *IEEE Microw. Mag.*, vol. 12, no. 7, pp. 78–94, Dec. 2011.

- [5] D. M. Sheen, D. L. McMakin, and T. E. Hall, "Three-dimensional millimeter-wave imaging for concealed weapon detection," *IEEE Trans. Microw. Theory Techn.*, vol. 49, no. 9, pp. 1581–1592, Sep. 2001.
- [6] X. Zhuze and A. G. Yarovoy, "Three-dimensional near-field MIMO array imaging using range migration techniques," *IEEE Trans. Image Process.*, vol. 21, no. 6, pp. 3026–3033, Jun. 2012.
- [7] J. Gao, Y. Qin, B. Deng, H. Wang, and X. Li, "Novel efficient 3D short-range imaging algorithms for a scanning 1D-MIMO Array," *IEEE Trans. Image Process.*, vol. 27, no. 7, pp. 3631–3643, Jul. 2018.
- [8] K. Mizuno, H. Matono, Y. Wagatsuma, H. Warashina, H. Sato, S. Miyana, and Y. Yamanaka, "New applications of millimeter-wave incoherent imaging," in *IEEE MTT-S Int. Microw. Symp. Dig.*, Long Beach, CA, USA, Jun. 2005, p. 4 and 632.
- [9] B. Larumbe, J. Laviada, A. Ibáñez-Loinaz, and J. Teniente, "Real-time imaging with frequency scanning array antenna for industrial inspection applications at W band," *J. Infr., Millim., THz Waves*, vol. 39, no. 1, pp. 45–63, Jan. 2018.
- [10] Q. Ma, D. S. Goshi, Y. C. Shih, and M. T. Sun, "An algorithm for power line detection and warning based on a millimeter-wave radar video," *IEEE Trans. Image Process.*, vol. 20, no. 12, pp. 3534–3543, Dec. 2011.
- [11] I. Nasr, R. Jungmaier, A. B. D. Noppeney, J. S. Bal, M. Wojnowski, E. Karagozler, H. Raja, J. Lien, I. Poupyrev, and S. Trotta, "A highly integrated 60 GHz 6-channel transceiver with antenna in package for smart sensing and short-range communications," *IEEE J. Solid-State Circuits*, vol. 51, no. 9, pp. 2066–2076, Sep. 2016.
- [12] Texas Instruments. (Mar. 2019). *77 GHz Radar-on-Chip for Short-Range Radar Applications*. [Online]. Available: <http://www.ti.com/product/AWR1642>
- [13] N. Llombart, K. B. Cooper, R. J. Dengler, T. Bryllert, and P. H. Siegel, "Confocal ellipsoidal reflector system for a mechanically scanned active terahertz imager," *IEEE Trans. Antennas Propag.*, vol. 58, no. 6, pp. 1834–1841, Jun. 2010.
- [14] S. S. Ahmed, A. Schiessl, and L.-P. Schmidt, "A novel fully electronic active real-time imager based on a planar multistatic sparse array," *IEEE Trans. Microw. Theory Techn.*, vol. 59, no. 12, pp. 3567–3576, Dec. 2011.
- [15] M. T. Ghasr, M. A. Abou-Khousa, S. Kharkovsky, R. Zoughi, and D. Pommerenke, "Portable real-time microwave camera at 24 GHz," *IEEE Trans. Antennas Propag.*, vol. 60, no. 2, pp. 1114–1125, Feb. 2012.
- [16] J. Laviada, A. Arboleya-Arboleya, Y. Alvarez, B. Gonzalez-Valdés, and F. Las-Heras, "Multiview three-dimensional reconstruction by millimetre-wave portable camera," *Sci. Rep.*, vol. 7, Jul. 2017, Art. no. 6479.
- [17] J. Laviada, A. Arboleya-Arboleya, and F. Las-Heras, "Multistatic millimeter-wave imaging by multiview portable camera," *IEEE Access*, vol. 5, pp. 19259–19268, 2017.
- [18] J. Laviada, M. López-Portugués, A. Arboleya-Arboleya, and F. Las-Heras, "Multiview mm-Wave imaging with augmented depth camera information," *IEEE Access*, vol. 6, pp. 16869–16877, 2018.
- [19] J. Laviada, F. Las-Heras, M. T. Ghasr, and R. Zoughi, "Multiview imaging with real-time microwave camera from known positions," in *Proc. IEEE Int. Symp. Antennas Propag.*, Boston, MA, USA, Jul. 2018, pp. 613–614.
- [20] H. He, P. Maheshwari, and D. J. Pommerenke, "The development of an EM-field probing system for manual near-field scanning," *IEEE Trans. Electromagn. Compat.*, vol. 58, no. 2, pp. 356–363, Apr. 2016.
- [21] H. He, V. Khilkevich, and D. Pommerenke, "2D imaging system with optical tracking for EMI source localization," in *Proc. IEEE Symp. Electromagn. Compat. Signal Integrity*, Mar. 2015, pp. 107–110.
- [22] C. Baer, J. Barowski, and I. Rolfes, "On the usability of low-cost inertial navigation systems for free-hand SAR imaging at GPR-frequencies," in *Proc. IEEE Sensors Appl. Symp. (SAS)*, Mar. 2017, pp. 1–5.
- [23] J. T. Case, M. T. Ghasr, and R. Zoughi, "Nonuniform manual scanning for rapid microwave nondestructive evaluation imaging," *IEEE Trans. Instrum. Meas.*, vol. 62, no. 5, pp. 1250–1258, May 2013.
- [24] OptiTrack. (Feb. 2019). *Optitrack Motion Capture System*. [Online]. Available: <http://www.optitrack.com>
- [25] M. Soumekh, *Synthetic Aperture Radar Signal Processing with MATLAB Algorithms*. Hoboken, NJ, USA: Wiley, 1999.
- [26] A. Meta, P. Hoogeboom, and L. P. Ligthart, "Signal processing for FMCW SAR," *IEEE Trans. Geosci. Remote Sens.*, vol. 45, no. 11, pp. 3519–3532, Nov. 2007.
- [27] J. Barowski, I. Rolfes, and C. Baer, "Real-time imaging system for millimeter wave synthetic aperture radar sensors," in *1st IEEE MTT-S Int. Microw. Symp. Dig.*, May 2017, pp. 1–3.
- [28] J. Detlefsen, A. Dallinger, S. Schelkshorn, and S. Bertl, "UWB millimeter-wave FMCW radar using Hubert transform methods," in *Proc. IEEE 9th Int. Symp. Spread Spectr. Techn. Appl.*, Aug. 2006, pp. 46–48.
- [29] Z. Wang, J. Li, and R. Wu, "Time-delay- and time-reversal-based robust capon beamformers for ultrasound imaging," *IEEE Trans. Med. Imag.*, vol. 24, no. 10, pp. 1308–1322, Oct. 2005.
- [30] M. Klemm, I. J. Craddock, J. A. Leendertz, A. Preece, and R. Benjamin, "Improved delay-and-sum beamforming algorithm for breast cancer detection," *Int. J. Antennas Propag.*, vol. 2008, Apr. 2008, Art. no. 761402.
- [31] J. Yang, J. Thompson, X. Huang, T. Jin, and Z. Zhou, "FMCW radar near field three-dimensional imaging," in *Proc. IEEE Int. Conf. Commun. (ICC)*, Jun. 2012, pp. 6353–6356.
- [32] G. Álvarez-Narciandi, J. Laviada, M. R. Pino, and F. Las-Heras, "Attitude estimation based on arrays of passive RFID tags," *IEEE Trans. Antennas Propag.*, vol. 66, no. 5, pp. 2534–2544, May 2018.
- [33] Vayyar. (May 2019). *System on Chip Specification*. [Online]. Available: <http://vayyar.com/technology/>



GUILLERMO ÁLVAREZ-NARCIANDI received the M.Sc. degree in telecommunication engineering from the University of Oviedo, Gijón, Spain, in 2016, where he is currently pursuing the Ph.D. degree (with the support of a FPU grant from the Spanish Government). He was a Visiting Student with Stanford University, CA, USA, in 2014. He received the Special Award to the Best Entrepreneurship Initiative from the XV Arquímedes National Contest, in 2017, for the development of a RFID-based location system. He received the 2015 EPIGI-JON Industrial Partners Society Award to the Best Applied Project for the development and testing of a hybrid RSS-inertial Indoor positioning system. He has coauthored a patent on attitude estimation using RFID technology. His main research interests include location systems, attitude estimation systems, RFID technology, radar systems, and imaging techniques.



MIGUEL LÓPEZ-PORTUGUÉS received the degree in computer science and the Ph.D. degree from the University of Oviedo, Spain, in 2008 and 2017, respectively, where he is currently a Research Assistant with the TSC-UNIOVI Group. His main research interests include parallel and high-performance computing, computer vision, and fast iterative methods applied to electromagnetic and acoustic scattering problems.



FERNANDO LAS-HERAS (M'86–SM'08) received the M.S. degree and Ph.D. degrees in telecommunication engineering from the Technical University of Madrid (UPM), in 1987 and 1990, respectively. He was a National Graduate Research Fellow, from 1988 to 1990. He was an Associate Professor with the Department of Signal, Systems, and Radiocommunications, UPM, from 1991 to 2000. Since 2003, he has been a Full Professor with the University of Oviedo, where he

was the Vice-Dean of telecommunication engineering with the Technical School of Engineering, Gijón, from 2004 to 2008. As of 2001, he heads the Signal Theory and Communications Research Group (TSC-UNIOVI), Department of Electrical Engineering, University of Oviedo. He was a Visiting Lecturer with the National University of Engineering, Peru, in 1996, a Visiting Researcher with Syracuse University, NY, USA, in 2000, and a short term Visiting Lecturer with ESIGELEC, France, from 2005 to 2011. He was the Telefónica Chair of RF Technologies, ICTs Applied to Environment, and ICTs and Smartcities with the University of Oviedo, from 2005 to 2015. He is a member of the Board of Directors of the IEEE Spain Section, from 2012 to 2015, a member of the Board of the IEEE Microwaves & Antennas Propagation Chapter (AP03/MTT17), from 2016 to 2017, a member of the Science, Technology, and Innovation Council of Asturias, in 2010, and the President of the Professional Association of Telecommunication Engineers, Asturias. He has led and participated in a great number of research projects. He has authored over 190 technical journal papers, mainly in the areas of antennas, propagation, metamaterials, and inverse problems with applications to antenna measurement (NF-FF, diagnostics, and holography), electromagnetic imaging (security and NDT) and localization, developing computational electromagnetics algorithms and technology on microwaves, millimeter wave, and THz frequency bands.



JAIME LAVIADA was born in Gijón, Spain. He received the M.S. degree in telecommunication engineering and the Ph.D. degree from the Universidad de Oviedo, Spain, in 2005 and 2010, respectively.

In 2006, he joined the Signal Theory and Communications Research Group, University of Oviedo, where he has been involved in multiple national and European projects as well as contracts with several companies. In 2015, he moved to the

Antennas Group, Universidad Pública de Navarra, with a national Post-doctoral fellowship in collaboration with several applied research projects. Finally, he moved back to the Universidad de Oviedo, where he is currently an Assistant Professor. In addition, he was a Visiting Scholar with the Electromagnetics and Communications Laboratory, Pennsylvania State University, from 2007 to 2008, and the Applied Microwave Nondestructive Testing Laboratory, Missouri S&T, in 2017. His research interests include numerical techniques applied to electromagnetic imaging, antenna measurements, the method of moments, and antenna pattern synthesis.

• • •